IEEE Access
Multidisciplinary | Rapid Review | Open Access Journal

Received February 10, 2019, accepted March 11, 2019, date of publication March 14, 2019, date of current version April 3, 2019.

Digital Object Identifier 10.1109/ACCESS.2019.2905005

Enhanced Holographic Microwave Imaging for MNP Target Tumor Detection

LULU WANG, (Member, IEEE)
Department of Biomedical Engineering, School of Instrument Science and Opto-Electronics Engineering, Hefei University of Technology, Hefei 230009, China
e-mail: lwang381@hotmail.com

This work was funded by the National Natural Science Foundation of China (Grant No. 61701159, JZ2017GJQN1131), the Natural Science Foundation of Anhui Province (Grant No. 101413246, JZ2017AKZR0129), the Fundamental Research Funds for the Central Universities (JZ2018HGTB0236), and the Ministry of Education of the Peoples Republic of China (Grant No. 2160311028).

ABSTRACT Holographic microwave imaging (HMI) has been proposed as a potential imaging tool for breast cancer detection. However, this method is not sensitive enough to small tumors especially when they located inside the fibro-glandular tissue. This paper investigates the possibility of the use of enhanced HMI to improve the quality of breast image and diagnostic sensitivity by applying magnetic nanoparticles (MNP). A numerical system, including a realistic breast model, 16-element transducer array, a 2-element magnetic coil array, and an image processing model, has been developed to evaluate the effectiveness of the enhanced HMI method for mapping of a dense breast. The numerical results demonstrated that the proposed method could detect the MNP target breast tumor and distinguish the small tumor from fibro-glandular tissue in a dense breast, which has the potential to develop a useful imaging tool for early breast cancer detection in the future.

INDEX TERMS Microwave imaging, diagnosis and therapy, magnetic nanoparticles, nanotechnology.

I. INTRODUCTION

Breast cancer is one of the most severe health issues in women worldwide [1]. Although X-ray mammography is the current standard breast imaging tool [2], it has some limitations, such as uses harmful radiations, unsuitable for pregnant women and dense breasts [3]. Microwave imaging (MI) is a relatively cost-effective and promising tool for the diagnosis of various diseases, including lung cancer [4], breast cancer [5]–[7], brain stroke [8], [9], heart disease [10], and bone cancer [11]. MI offers morpho-functional evidence without producing harmful radiations. MI for abnormal tissue detection is highly dependent on the dielectric properties (DP, permittivity, and conductivity) contrast between the abnormal and healthy tissues at microwave spectrums. However, the MI-based techniques have some drawbacks, including limited image resolution, long scanning time, high computation cost, and less sensitive to small tumors [12]. Many researchers have proposed various new methods to solve these limitations.

Jiang *et al.* [13] investigated ultrasound-guided microwave imaging by combining the advantages of ultrasound and MI approaches to improve image resolution. Scapaticci *et al.* [14] developed molecular imaging to produce images of internal physiological or pathological processes in cells. The authors also developed a holographic microwave imaging (HMI) for imaging of biological object [15], [16]. However, this approach has difficulty in accurately distinguishing small inclusions (less than 5mm in diameter) especially when they embedded into fibro-glandular and dense tissues.

In the past decade, magnetic nanoparticles (MNP) have attracted much interest in biomedical imaging, diagnostics, and therapies [17]–[20]. The use of MNP in biomedicine and biotechnology has been growing dramatically [21], [22]. The recent development of the MNP imaging technique resulted in a new generation of nanocomposites with enhanced DP contrast between abnormal and healthy tissues. Clinical studies have confirmed MNP (e.g., Fe_3O_4) can be used as a contrast agent in biomedical imaging tools to reconstruct the MNP target cancer cells, which enables to prevent any ambiguity in identifying cancerous and fibroconnective tissues [23]–[26].

The MNP targeting technique includes delivering MNP to a target interest region and capturing them via an external magnetic field to the target region. The prior information on cancer cells is not required in the MNP delivering

The associate editor coordinating the review of this manuscript and approving it for publication was Andrei Muller.

process. By applying an external magnetic field, the drug-carried MNP can be delivered to the target interest region (e.g., tumors) without full circulation in the human body, which reduces curing time and minimizes dosages and side effects. Biomedical nanoparticles have increased the ability to accurately and effectively diagnose and treat various diseases including breast cancer [27] and Alzheimer's disease [28], [29]. The targeting MNP technique can only deliver a low volumetric concentration of MNP to the target region.

This paper investigates the feasibility of the use of an enhanced HMI approach for imaging of MNP target breast tumor. A realistic numerical system was developed using MATLAB software to demonstrate the proof-of-concept of the proposed framework. Various numerical experiments on a realistic human breast phantom were conducted to evaluate the proposed method in realistic conditions, in which the MNP behavior has been modeled according to the results of an experimental characterization.

II. MAGNETIC SUSCEPTIBILITY OF MNP

MNP is often considered as ferrofluids (FF) in biomedical applications. The magnetization dynamics of MNP can be modeled by [30]:

$$\tau_N = \tau_0 e^{\frac{K_a V_m}{k_b T}} \tag{1}$$

where τ_0 denotes the characteristic time, K_a is the anisotropy constant, V_m is the magnetic core volume of each MNP, k_b and T are the Boltzmann constant and the absolute temperature.

The Brownian relaxation is caused by the mechanical rotation of the MNP in the carrier liquid.

$$\tau_B = \frac{3\eta V_H}{k_b T} \tag{2}$$

where η is the viscosity of the carrier liquid and V_H is the hydrodynamic volume of MNP.

The relaxation time of the magnetization decay of an FF is:

$$\tau_{eff} = \frac{\tau_N \tau_B}{\tau_N + \tau_B} \tag{3}$$

The complex susceptibility of an FF can be defined as [31]:

$$x_\mu(\omega) = \frac{1}{3}[x_\parallel(\omega) + 2x_\perp(\omega)] \tag{4}$$

where $x_\parallel$ and $x_\perp$ are the parallel susceptibility and transverse susceptibility, respectively. $x_\parallel$ is related to the low frequency (relaxation mechanisms) contribution, and $x_\perp$is related to high frequency (ferromagnetic resonance) contribution [32]. The proposed system uses relatively low operation frequency (low GHz range), then the parallel susceptibility can be neglected. In this case, x_μ can be represented as [26]:

$$x_\mu(\omega) \approx \frac{2}{3}x_\perp(\omega) = \frac{2}{3}x_0 \frac{1 + (\omega_0\tau_0)^2 + i\omega\tau_0}{1 + (\omega_0\tau_0)^2 - (\omega\tau_0)^2 + 2i\omega\tau_0} \tag{5}$$

where x_0 is the static transverse susceptibility, τ_0 denotes characteristic time, ω is the angular frequency, $\omega_0 = \gamma H_a$, where γ is the gyromagnetic ratio, H_a is the anisotropy field $H_a = 2K_a/(\mu_0 M_s)$, μ_0 is the permeability of free-space.

Equation (5) is valid when a PMF with amplitude H is superimposed to the time harmonic EM field, which is dependent on x_0 and ω_0. In particular, ω_0 increases [33]:

$$\omega_0(H) = \gamma(H_a + H) \tag{6}$$

While x_0 decreases as:

$$x_0(H) = \frac{cM^2 V_m \mu_0}{k_b T}\left[\frac{\coth\left(\frac{mH}{k_b T}\right)}{\frac{mH}{k_b T}} - \frac{1}{\left(\frac{mH}{k_b T}\right)^2}\right] \tag{7}$$

where m is the magnetic moment amplitude of MNP, and c means the volumetric concentration of MNP.

III. METHOD

A. ENHANCED HMI SYSTEM

Figure 1 displays a conceptual scheme of the fully programmable enhanced HMI system for MNP target tumor detection. The system contains an EM source generator, an imaging scanner consists of a 3D breast model containing MNP target tumor and an N-element transducer array, a pair of magnetic coils to generate a polarizing magnetic field (PMF), and a fast computer with image program tool. All transducers are positioned on the same 2D plane, and each transducer works as both transmitter and detector. The magnetic coils are placed on the top and bottom of the scanner, respectively. A matching medium is filled in the space between the object and the transducers.

During data collection, the EM source generator generates EM field to the magnetic coils and N-element transducer array at microwave frequencies. Each magnetic coil transmits a PMF to the MNP target tumor (consists of electric and magnetic contrasts), each transducer transmits and measures the EM fields to/from the breast. The magnetic susceptibility of MNP is almost negligible at microwave frequencies for a PMF of sufficient strength. The MNP can be modified and monitored by changing the PMF values, which offers useful information. The imaging procedure includes two main steps: 1) generate time-harmonic EM waves to the MNP target interest region (such as a tumor) and extracted useful signals from the scattered signals; 2) reconstruct the MNP target tumor from the extracted signals using the proposed imaging algorithm. No significant variation occurs in the measurement setup due to high-speed data measurement processing.

B. FORWARD PROBLEM

We can present the total electric and magnetic fields inside the breast contains electric and magnetic contrast

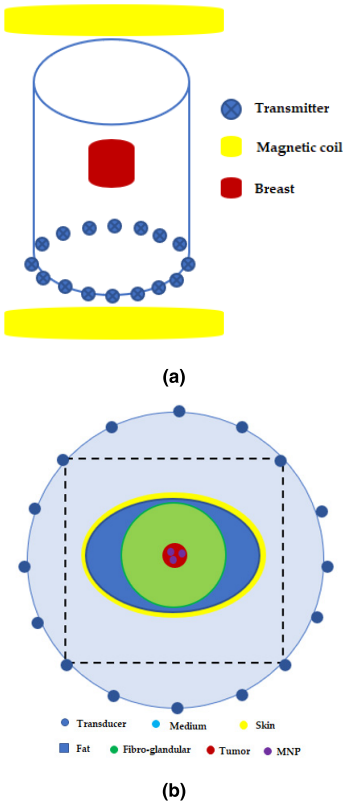

FIGURE 1. (a) Enhanced HMI configuration; (b) breast model and transducer array configuration.

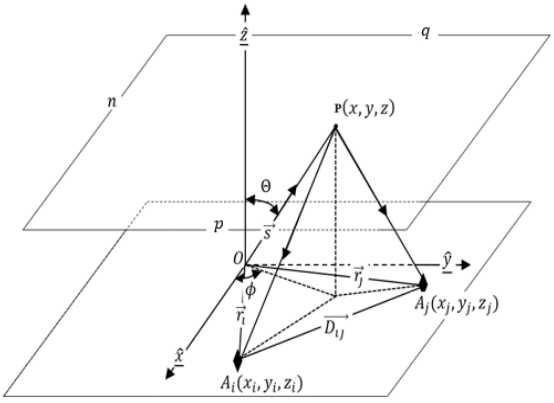

FIGURE 2. Measurement setup of two transducers.

as [34]:

$$\vec{E}(\vec{r}) = \vec{E}_{inc}(\vec{r}) + [k_b^2 + \nabla\nabla\cdot] \int_V G\left(\vec{r}, \vec{r}'\right) \Delta x_E\left(\vec{r}'\right) \times \vec{E}\left(\vec{r}'\right) dV - j\omega\mu_b \nabla \times \int_V \mathrm{G}\left(\vec{r}, \vec{r}'\right) \Delta x_H\left(\vec{r}'\right) \vec{H}\left(\vec{r}'\right) dV \quad (8)$$

$$\vec{H}(\vec{r}) = = \vec{H}_{inc}(\vec{r}) + [k_b^2 + \nabla\nabla\cdot] \int_V G\left(\vec{r}, \vec{r}'\right) \Delta x_H\left(\vec{r}'\right) \times \vec{H}\left(\vec{r}'\right) dV - j\omega\tilde{\varepsilon}_b \nabla \times \int_V \mathrm{G}\left(\vec{r}, \vec{r}'\right) \Delta x_E\left(\vec{r}'\right) \vec{E}\left(\vec{r}'\right) dV \quad (9)$$

where $\vec{r}$ denotes the transducer/coil located at $\vec{r}$, $\vec{r}'$ denotes the transducer/coil located at $\vec{r}'$, ω is the angular frequency, k_b and μ_b are the wavenumber and magnetic permeability of background, respectively. $\mathrm{G}\left(\vec{r}, \vec{r}'\right)$ is the Green's function, $\mathrm{G}\left(\vec{r}, \vec{r}'\right) = e^{-jk_b\left|\vec{r}-\vec{r}'\right|}/4\pi\left|\vec{r}-\vec{r}'\right|$, Δx_E and Δx_H are the electric and magnetic contrasts, $\Delta x_E = (\tilde{\varepsilon}(\vec{r}) - \tilde{\varepsilon}_b)/\tilde{\varepsilon}_b$, $\Delta x_H = (\mu(\vec{r}) - \mu_b)/\mu_b$, here $\tilde{\varepsilon}(\vec{r})$ is the complex permittivity of the object and $\tilde{\varepsilon}_b$ is the complex permittivity of the background. $\tilde{\varepsilon}(\vec{r}) = \varepsilon(\vec{r}) - j\sigma(\vec{r})/\omega$, $\tilde{\varepsilon}_b(\vec{r}) = \varepsilon_b(\vec{r}) - j\sigma_b(\vec{r})/\omega$, ε_b is the relative permittivity of background, σ_b and σ denote the conductivities of the background and the object, respectively. μ_b and μ are the permeabilities of the background and the object, respectively. $\vec{E}_{inc}$ denotes the incident electric field illuminates to the object, and $\vec{H}$ denotes the magnetic field introduced to the target object.

The above equation can be simplified as:

$$\vec{E}_{inc}(\vec{r}) = \vec{E}(\vec{r}) + j\omega\vec{A}(\vec{r}) + \frac{j\omega}{k_b^2}\nabla\nabla\cdot\vec{A}(\vec{r}) + \frac{\nabla\times\vec{F}(\vec{r})}{\tilde{\varepsilon}_b} \quad (10)$$

$$\vec{H}_{inc}(\vec{r}) = \vec{H}(\vec{r}) + j\omega\vec{F}(\vec{r}) - \frac{j\omega}{k_b^2}\nabla\nabla\cdot\vec{F}(\vec{r}) + \frac{\nabla\times\vec{A}(\vec{r})}{\mu_b} \quad (11)$$

where magnetic vector potential $\vec{A}(\vec{r}) = j\omega\mu_b\tilde{\varepsilon}_b \int_V \mathrm{G}\left(\vec{r}, \vec{r}'\right) \Delta x_E\left(\vec{r}'\right) \vec{E}\left(\vec{r}'\right) dV$, and electric vector potential $\vec{F}(\vec{r}) = j\omega\mu_b\tilde{\varepsilon}_b \int_V \mathrm{G}\left(\vec{r}, \vec{r}'\right) \Delta x_H\left(\vec{r}'\right) \vec{H}\left(\vec{r}'\right) dV$.

C. BACKWARD PROBLEM

The scattered electric and magnetic fields from the MNP target region can be modeled as:

$$\vec{E}_{scat}(\vec{r}_i) = \int_V \left(k_b^2 + \nabla\nabla\cdot\right) G\left(\vec{r}_i, \vec{r}'\right) \Delta x_E\left(\vec{r}'\right) \vec{E}\left(\vec{r}', \vec{r}_t\right) dV - j\omega\mu_b \int_V \nabla\times \mathrm{G}\left(\vec{r}_i, \vec{r}'\right) \Delta x_H\left(\vec{r}'\right) \vec{H}\left(\vec{r}', \vec{r}_t\right) dV \quad (12)$$

$$\vec{H}_{scat}(\vec{r}_i) = \int_V \left(k_b^2 + \nabla\nabla\cdot\right) G\left(\vec{r}_i, \vec{r}'\right) \Delta x_H\left(\vec{r}'\right) \vec{H}\left(\vec{r}', \vec{r}_t\right) dV + j\omega\tilde{\varepsilon}_b \int_V \nabla\times \mathrm{G}\left(\vec{r}_i, \vec{r}'\right) \Delta x_E\left(\vec{r}'\right) \vec{E}\left(\vec{r}', \vec{r}_t\right) dV \quad (13)$$

where $\vec{r}_i$ denotes the transducer located at $\vec{r}_i$. The above equation can be represented by using the electric and magnetic

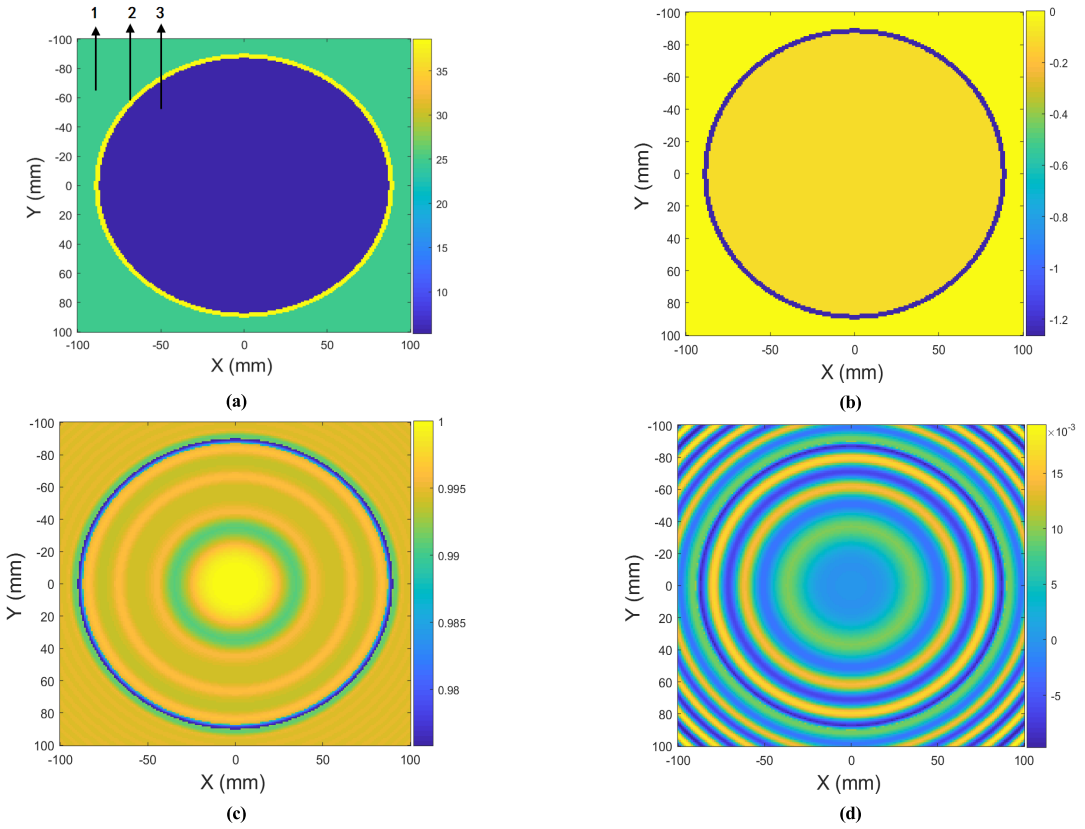

FIGURE 3. 2D view of breast model I: (a) real-part (relative permittivity), (b) imagery-part (conductivity); 2D view of reconstructed images of breast model I: (c) real-part; (d) imagery-part. (1: matching medium, 2: skin, 3: fat).

dyadic Green's functions:

$$\vec{E}_{scat}(\vec{r}_i) = k_b^2 \int_V \mathrm{G}_b^E\left(\vec{r}_i, \vec{r}'\right) \Delta x_E\left(\vec{r}'\right) \vec{E}\left(\vec{r}', \vec{r}_t\right) dV - j\omega\mu_b \int_V \mathrm{G}_b^H\left(\vec{r}_i, \vec{r}'\right) \Delta x_H\left(\vec{r}'\right) \vec{H}\left(\vec{r}', \vec{r}_t\right) dV \quad (14)$$

$$\vec{H}_{scat}(\vec{r}_i) = k_b^2 \int_V \mathrm{G}_b^E\left(\vec{r}_i, \vec{r}'\right) \Delta x_H\left(\vec{r}'\right) \vec{H}\left(\vec{r}', \vec{r}_t\right) dV + j\omega\tilde{\varepsilon}_b \int_V \mathrm{G}_b^H\left(\vec{r}_i, \vec{r}'\right) \Delta x_E\left(\vec{r}'\right) \vec{E}\left(\vec{r}', \vec{r}_t\right) dV \quad (15)$$

where $\mathrm{G}_b^E\left(\vec{r}_i, \vec{r}'\right)$ and $\mathrm{G}_b^H\left(\vec{r}_i, \vec{r}'\right)$ are the electric and magnetic dyadic Green's functions, respectively.

$$\mathrm{G}_b^E\left(\vec{r}_i, \vec{r}'\right) = \frac{e^{-jk_bR}}{4\pi R^3} \times \begin{bmatrix} h_1+(x-x')^2h_2 & (x-x')(y-y')h_2 & (x-x')(z-z')h_2 \\ (x-x')(y-y')h_2 & h_1+(y-y')^2h_2 & (y-y')(z-z')h_2 \\ (x-x')(z-z')h_2 & (y-y')(z-z')h_2 & h_1+(z-z')^2h_2 \end{bmatrix},$$

$$\mathrm{G}_b^H\left(\vec{r}_i, \vec{r}'\right) = -\frac{(1+jk_bR)e^{-jk_bR}}{4\pi R^3} \begin{bmatrix} 0 & -(z-z') & (y-y') \\ (z-z') & 0 & -(x-x') \\ -(y-y') & (x-x') & 0 \end{bmatrix},$$

$R = \left|\vec{r}_i - \vec{r}'\right|$, $h_1 = R^2(1 + \frac{1}{jk_bR} - \frac{1}{(k_bR)^2})$, and $h_2 = (-1 - \frac{3}{jk_bR} + \frac{3}{(k_bR)^2})$.

Equations (14) and (15) can be used to model the scattered EM fields as long as the working frequency is relatively low. The conductivity of biological tissue is relatively small compared to good conducting materials, e.g., metals. The Born approximation can be used to solve the forward problem. Therefore, the EM fields inside the object can be considered approximately as the incident field that exists at the same location without presenting the object. Equation (14) changes to:

$$\vec{E}_{scat}\left(\vec{r}_i\right) = k_b^2 \int_V \mathrm{G}_b^E\left(\vec{r}_i, \vec{r}'\right) \Delta x_E\left(\vec{r}'\right) \vec{E}_{inc}\left(\vec{r}_i, \vec{r}'\right) dV - j\omega\mu_b \int_V \mathrm{G}_b^H\left(\vec{r}_i, \vec{r}'\right) \Delta x_H\left(\vec{r}'\right) \vec{H}_{inc}\left(\vec{r}_i, \vec{r}'\right) dV \quad (16)$$

The scattered electric field is much smaller than the incident electric field if the permeability of MNP is much smaller

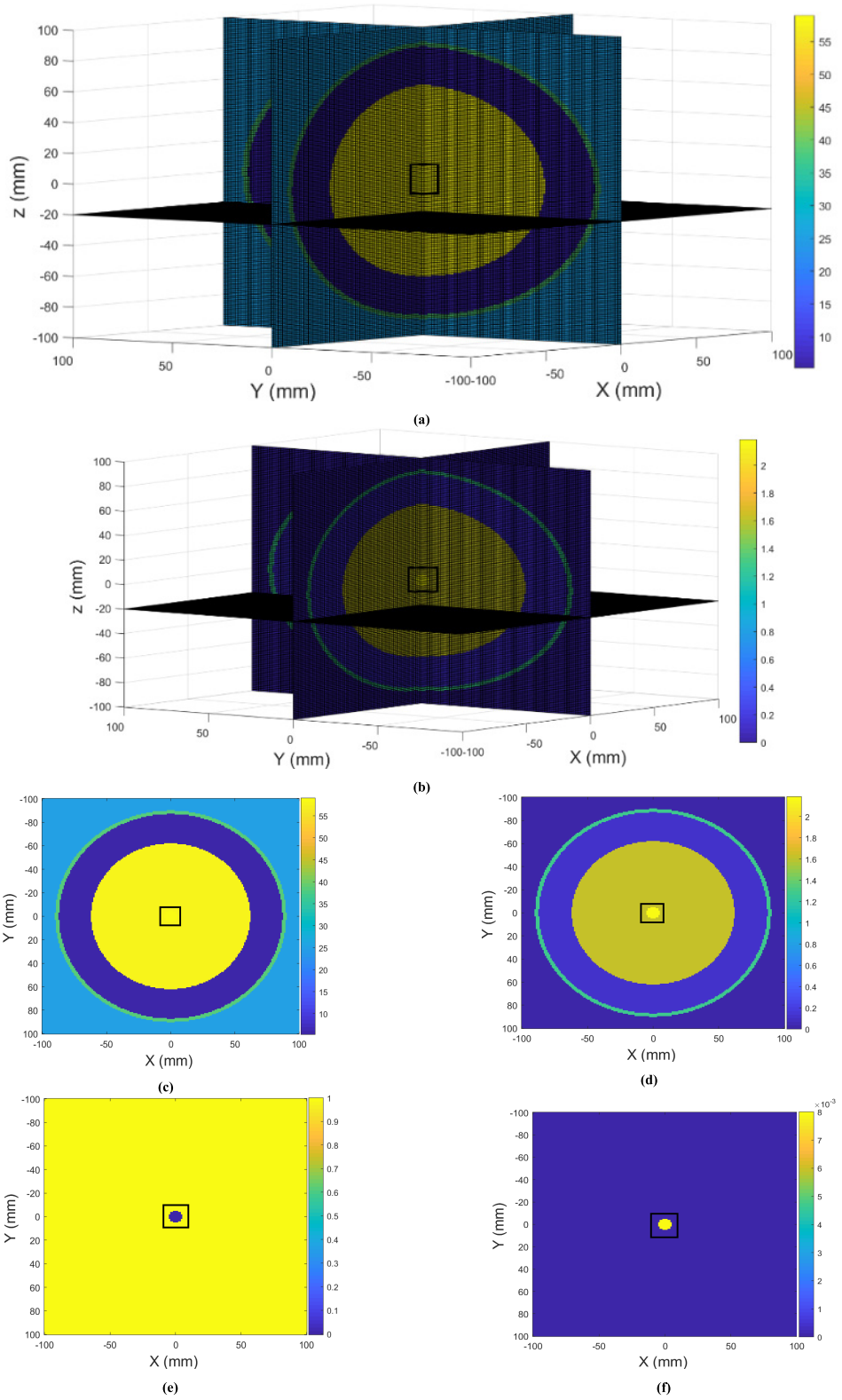

FIGURE 4. 3D views of the breast model II: (a) real-part (relative permittivity), (b) imagery-part (conductivity); 2D views of the breast model II: (c) real-part (relative permittivity), (d) imagery-part (conductivity); Permeability distribution of breast model II: (e) real-part, (f) imagery-part; 2D reconstructed images of breast model II.

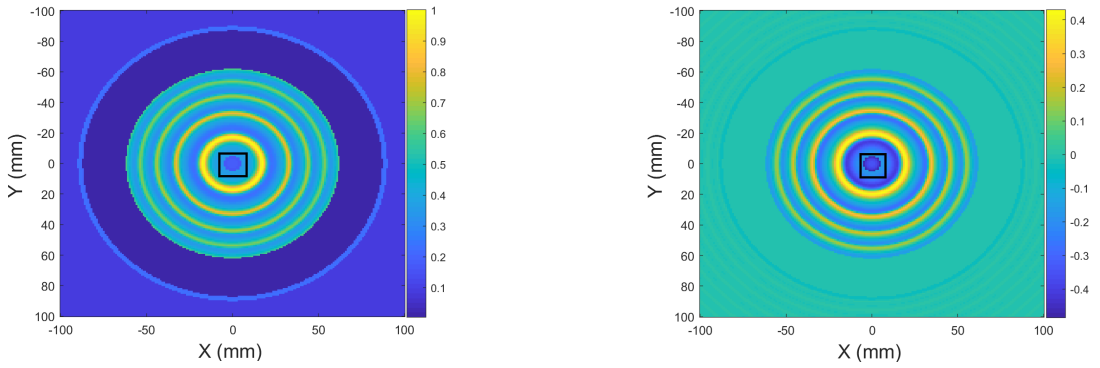

FIGURE 4. *(Continued.)* **(g) real-part; (h) imagery-part.**

than that of the object. The MNP can be reconstructed if the scattered field can be extracted from the incident field. Moreover, the MNP can be reconstructed from the scattered electric field by solving the linear inversion procedure.

D. IMAGE PROCESSING

As shown in Figure 2, a target point P is assumed inside the breast containing MNP, the cross-correlation of the scattered electric fields measured by any pair of transducers located at A_i and A_j can be computed as visibility data [35]:

$$\vec{V}_{vi}\left(\vec{r}_i, \vec{r}_j\right) = < \vec{E}_{scat}(\vec{r}_i) \cdot \vec{E}^*_{scat}(\vec{r}_j) > \tag{17}$$

where $<>$ denotes the time average, $\vec{E}_{scat}(\vec{r}_i)$ and $\vec{E}^*_{scat}(\vec{r}_j)$ are the scatted electric field and the conjugate complex of the scatted electric field measured by the receivers located at $\vec{r}_i$ and $\vec{r}_j$, respectively. The total visibility data is $\vec{V} = \sum_i^N \vec{V}_{vi}$, $i \neq j$, $N \geq 3$, N is the total number of transducers.

We defined breast intensity as [36]:

$$\mathrm{I}\left(\vec{s}\right) = \left(\frac{\mathrm{j}\omega\mu_0}{4\pi}\right)^2 |\sigma + \mathrm{j}\omega\varepsilon_0\varepsilon_\mathrm{r} - \sigma_b|^2 \vec{E}\left(\vec{s}\right) \cdot \vec{E}^*\left(\vec{s}'\right) \tag{18}$$

where ε_0 and ε_r denote the relative permittivity of free-space and object, respectively.σ and σ_b are conductivities of the object and background, respectively. μ_0 denotes the magnetic permeability of free-space.

The visibility data over the breast can be computed using the following equation:

$$\vec{V}_{vi}\left(\vec{r}_i, \vec{r}_j\right) = \left(\frac{j\omega\mu_0}{4\pi}\right)^2 \iiint_{\mathbf{V}} |\sigma + j\omega\varepsilon_0\varepsilon_\mathrm{r} - \sigma_b|^2 \vec{E}\left(\vec{s}\right) \cdot \vec{E}^*(\vec{s}) \frac{e^{-jk_0(\vec{r}_i - \vec{r}_j)\cdot\hat{\underline{s}}}}{s^2} \tag{19}$$

The visibility data can be simplified by combining (18) and (19):

$$\vec{V}_{vi}\left(\vec{D}_{ij}\right) = \iiint_v I(\vec{s}) \frac{e^{-j2\pi\vec{D}_{ij}\cdot\hat{\underline{s}}}}{s^2} dV \tag{20}$$

where $\vec{D}_{ij} = (\vec{r}_j - \vec{r}_i)/\lambda_b$, λ_b is the wavelength of the background, $\hat{\underline{s}} = sin\theta cos\phi\hat{\underline{x}} + sin\theta sin\phi\hat{\underline{y}} + cos\theta\hat{\underline{z}}$, $dV = s^2 sin\theta d\theta d\phi ds$, which can be represent as $dV = s^2 dldmds/n$. Here, $l = sin\theta cos\phi$, $m = sin\theta sin\phi$, and $n = cos\theta = \sqrt{1 - l^2 - m^2}$. Thus, the visibility formula can be represented as:

$$\vec{V}_{vi}\left(\vec{u}_{ij}, \vec{v}_{ij}, \vec{w}_{ij}\right) = \int_l \int_m \int_n \frac{I(s, l, m)}{\sqrt{1 - l^2 - m^2}} e^{-j2\pi\Phi_{ij}} dldmds \tag{21}$$

where $\Phi_{ij} = \vec{D}_{ij} \cdot s = \vec{u}_{ij}l + \vec{v}_{ij}m + \vec{w}_{ij}n$.

The visibility data can be rewritten as the following equation if all transducers are located on the same flat plane ($\vec{w}_{ij} = 0$).

$$\vec{V}_{vi}\left(\vec{u}_{ij}, \vec{v}_{ij}\right) = \iint I(l, m) e^{-j2\pi(\vec{u}_{ij}l + \vec{v}_{ij}m)} \tag{22}$$

A 2D image of the 3D breast model can be mapped by taking an inverse Fourier transform of (22):

$$(l, m) = \iint \vec{V}_{vi}\left(\vec{u}_{ij}, \vec{v}_{ij}\right) e^{j2\pi(\vec{u}_{ij}l + \vec{v}_{ij}m)} dudv \tag{23}$$

E. METRIC

In this study, the peak signal-to-noise ratio (PSNR) has been used to serve as objective criteria:

$$PSNR = 10log_{10}(255/\sqrt{MSE}) \tag{24}$$

where MSE (mean squared error) is the quality estimator, it is non-negative. The MSE value much closer to zero demonstrates a better performance.

IV. NUMERICAL EXPERIMENTS

A numerical system (see Figure 1) was developed to demonstrate the enhanced HMI method for imaging the distribution of MNP target tumors embedded in a realistic breast model. Several simulations were performed to investigate the effectiveness, sensitivity, and accuracy of the proposed method. All simulations were performed using MATLAB 2018a (The MathWorks, Inc. Natick, MA)

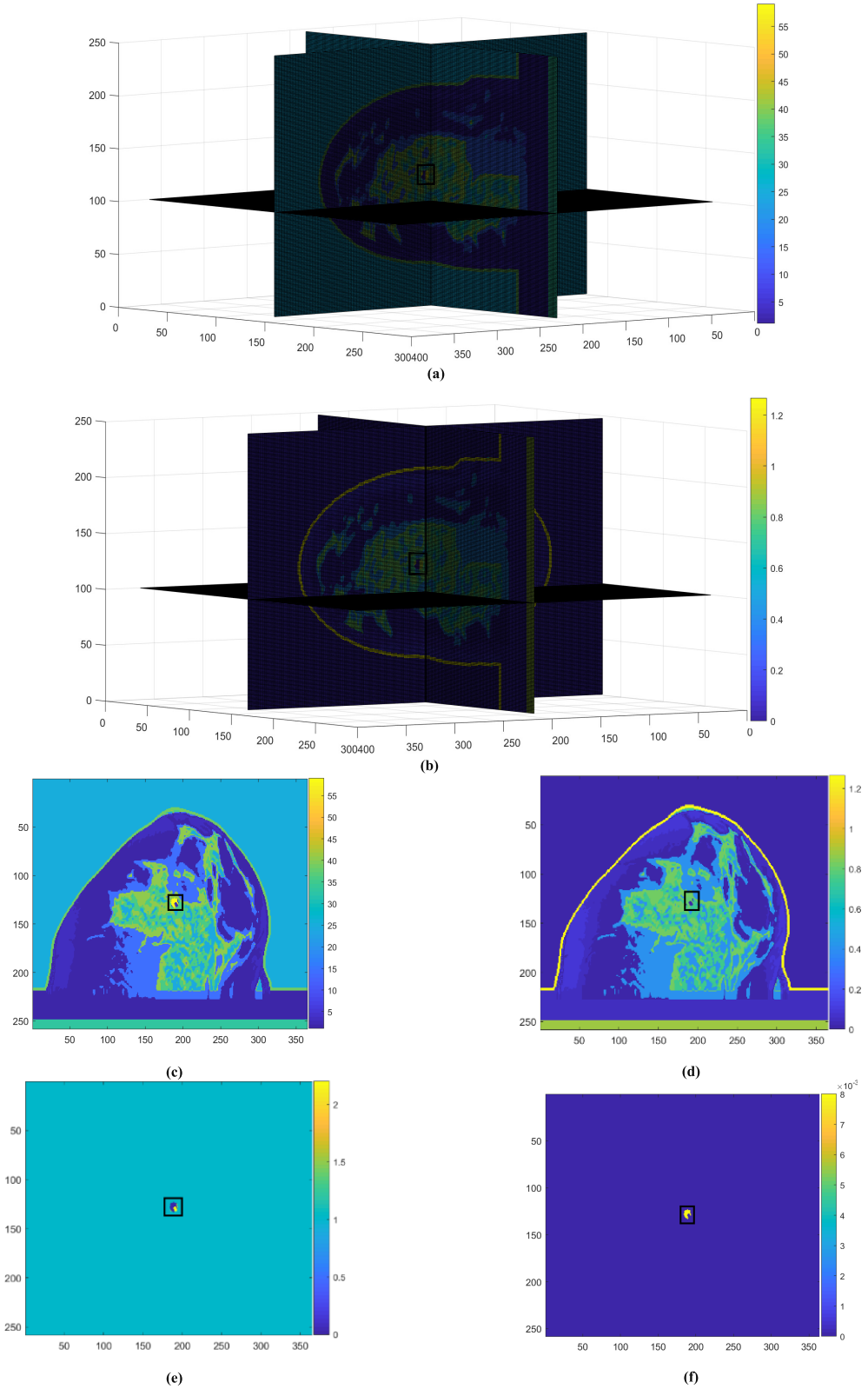

FIGURE 5. Breast model III: (a) 3D view of real-part (relative permittivity), (b) 3D view of imagery-part (conductivity); (c) 2D view of real-part (relative permittivity); (d) 2D view of imagery-part (conductivity); permittivity distribution of breast model III (e) real-part, (f) imagery-part; 2D view of reconstructed images of breast model III.

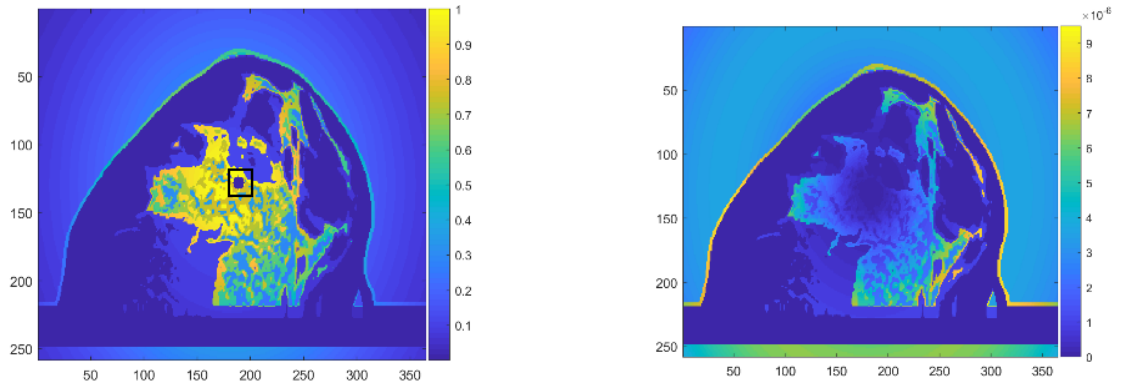

(g) (h)

FIGURE 5. *(Continued.)* **(g) real-part; (h) imagery-part.**

on a Dell Precision 5820 workstation with Intel Xeon W-2145 CPU at 3.7 GHz and 256 GB of RAM.

According to previous studies [15], [16], [26], the breast phantom was placed on the top of the 16-element transducer array, and all transducers were enclosed by the cubic shield and a matching medium ($\varepsilon_b = 25$, $\sigma_b = 0$S/m, $\mu_b = 1$) was filled in the space between the object and the transducer array, and the single frequency of 2GHz was chosen as the working frequency [33]. During image data collection, the model and the transducer array were positioned at z=0mm and z=−60mm ($2\lambda_b$) and a 2D image data set was recorded to produce a 2D image [15].

A. FORWARD SOLUTION

In the forward simulation, a waveguide antenna was modeled as a transmitter to radiate microwave signals into the breast phantom using the finite difference time domain (FDTD) method. The incident electric field radiated from such a transmitter can be modeled as:

$$\vec{E}_{inc}\left(\vec{T}_{x_m}\right) = \left(-\frac{jk_0}{2\pi^2}\right)\vec{E}_0\left(\frac{e^{-jk_0\vec{R}_{\vec{T}_{x_m}}}}{\vec{R}_{\vec{T}_{x_m}}}\right)h\left(\theta,\emptyset\right)\vec{P}(\theta,\emptyset)A_N B_B \quad (25)$$

where $\vec{R}_{\vec{T}_{x_m}}$ is the vector position from the object to the transmitter located at $\vec{T}_{x_m}$, $\vec{E}_0$ is the wave amplitude of TE10 mode, $h\left(\theta,\emptyset\right)$ is the radiation pattern, and $\vec{P}(\theta,\emptyset)$ is the polarization vector. A_N and B_B are the narrow and board aperture dimensions of the antenna, respectively, $A_N = 10$mm and $B_B = 20$mm were chosen in simulation setups.

B. BACKWARD SOLUTION

The same waveguide antenna was also simulated to measure the scattered electric field from the breast in the backward simulation. We applied the Born Approximation to determine the scattered electric field, then the electric field and magnetic fields inside the breast can be modeled approximately as the incident fields that exist at the same location but without the breast presented in the imaging domain. The scattered electric field from the breast can be measured by any transducer located at $\vec{r}_m$:

$$\vec{E}_{scat}\left(\vec{r}_m\right) = k_b^2\int_V \mathrm{G}_b^E\left(\vec{r}_m,\vec{s}\right)\Delta x_E\left(\vec{s}\right)\vec{E}_{inc}\left(\vec{T}_{x_m},\vec{s}\right)dV - j\omega\mu_b\int_V \mathrm{G}_b^H\left(\vec{r}_m,\vec{s}\right)\Delta x_H\left(\vec{s}\right)\vec{H}_{inc}\left(\vec{T}_{x_m},\vec{s}\right)dV \quad (26)$$

The single circle loop coil was modeled as an excitation magnetic coil to transmit the PMF field. The magnetic field induced by each excitation coil can be calculated by:

$$\vec{H}_{inc} = \frac{\mu_0 I}{4\pi r_c^2}\oint dL = \frac{\mu_0 I}{4\pi r_c^2}2\pi r_c = \frac{\mu_0 I}{2r_c} \quad (27)$$

where I is the current in the coil, r_c and L are the radius and length of the coil. The current of 1A was chosen for the simulation setup.

The scattering electric field was numerically measured using the N-element transducer array, and the total number of $N \times (N-1)$ data was recorded to produce an MNP target breast image using the developed algorithm.

C. BREAST MODEL

As shown in Figures 3-7 and Table 1, we developed five sphere-shaped breast models using MATLAB software to demonstrate the working principle of the enhanced HMI method. Breast models I and II ($200 \times 200 \times 200$ voxels) were developed using Gaussian function, while breast models III and IV ($256 \times 365 \times 248$ voxels) were developed using MRI images and taken from the Wisconsin University Repository which was a dense breast (ID: 070604PA2) [37].

A sphere-shaped tumor with a radius of 5mm (squared in black) was positioned in two locations in the breast models: inside the fibro-glandular tissue and the fat tissue. In breast model IIs and III, the MNP target tumor ($\varepsilon_r = 59.022$, $\sigma_r = 2.1861$ S/m) was emulated inside the fibro-glandular tissue

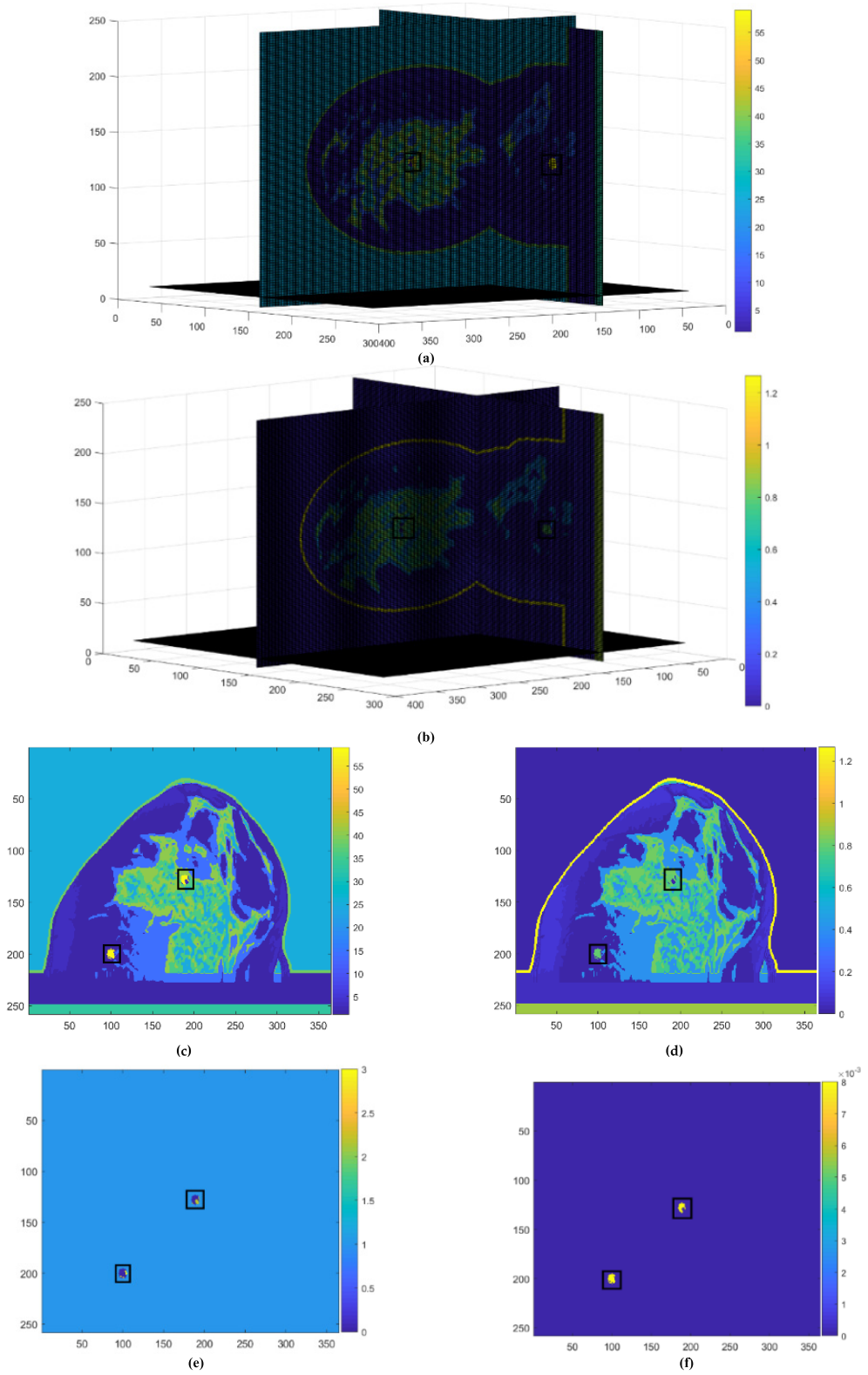

FIGURE 6. 3D views of breast model IV: (a) real-part (relative permittivity), (b) 3Imagery-part (conductivity); 2D views of breast model IV: (c) real-part (relative permittivity); (d) imagery-part (conductivity); permeability distribution of breast model IV (e) real-part, (f) imagery-part; reconstructed breast images.

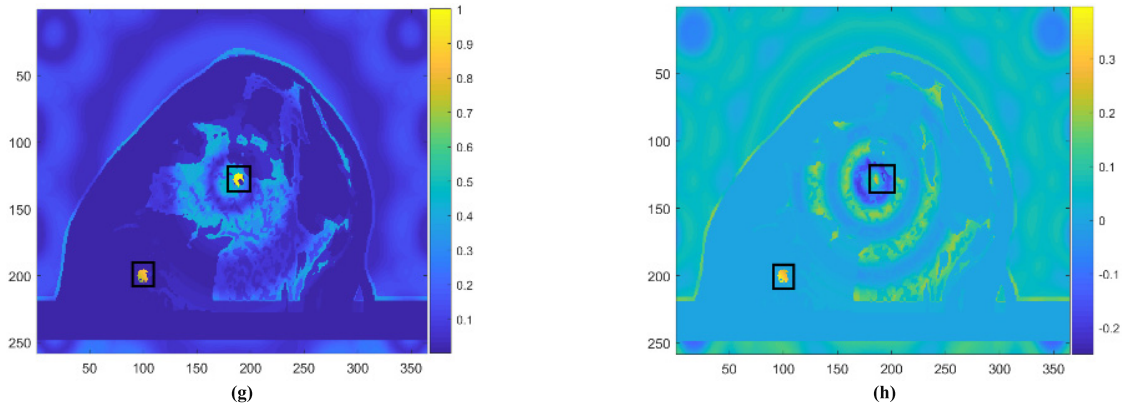

FIGURE 6. *(Continued.)* **(g) real-part; (h) imagery-part.**

in the slices 100 and 124 of the model, respectively. In breast models IV and V, the two MNP target tumors ($\varepsilon_r = 60, \sigma_r = 0.8$ S/m) were embedded in fibro-glandular and fat tissues in the slice 124 of the breast.

Considering MNP with a magnetic core diameter of 10 nm (e.g., $V_m \approx 0.5 \times 10^{-24}$ m^3) and a cell diameter of 10 μm (e.g., $V_{cell} \approx 0.5 \times 10^{-15}$m^3), for typical cellular uptake$\alpha \approx 10^6 \sim 10^7$ particles [38], a volumetric concentration ($c = \alpha V_m / V_{cell}$) is less than 0.1–1%. According to equations (5)-(7) and the published physical parameters [26], the MNP with a magnitude $|\Delta x_\mu|$ of 0.008 for H=0 kA/m. A matching solution medium ($\varepsilon_b = 25, \sigma_b = 0$ S/m, $\mu_b = 1$) was used in the space between the breast and the transducer array to reduce noises.

V. RESULTS

Several numerical simulations have been conducted to test the possibility of the enhanced HMI for identifying MNP target tumors embedded in a realistic breast. The region under test is a cubic (200 mm^3 in size) including breast model and matching fluid medium (see Table 1). Both noise-free and noise models were involved in this numerical study.

In the first test, the simplified breast model consisted of skin and fat. Figures 3(a)-(b) show the real-part (relative permittivity) and imaginary-part (conductivity) of breast model I, while Figures 3 (c)-(d) present the real-part and imaginary-part of the reconstructed images of the breast model I. The internal structures of the breast can be identified in the real-part of the reconstructed image.

The second breast model under test consisted of a layer of skin, fat, fibro-glandular and one MNP target tumor ($\varepsilon_r = 59.022, \sigma_r = 2.1861$ S/m, $\mu_r = -0.005 - 0.008$i). The tumor (0 mm, 0 mm, 0 mm) was embedded in the fibro-glandular tissue. The DPs of the tumor are very similar to that of fibro-glandular tissue ($\varepsilon_r = 57.85, \sigma_r = 1.6333$ S/m, $\mu_r = 1$). Figures 4(a)-(d) show the 2D and 3D reviews of the real-part and imaginary-part of the breast model II. Figure 4(e) and Figure 4(f) displays the real-part and imaginary-part of the permeability distributions of the breast

TABLE 1. Breast models and DP of tissues at 2GHz [16].

Breast Model	Structures	σ (S/m)	Relative Permittivity	Permeability
I	Medium	0	25	1
	Skin	1.2654	38.568	1
	Fat	0.10612	5.2323	1
II	Medium	0	25	1
	Skin	1.2654	38.568	1
	Fat	0.10612	5.2323	1
	Fibro-glandular	1.6333	57.85	1
	Tumor	2.1861	59.022	-0.005-0.008i
III & IV	Medium	0	25	1
	Muscle	0.866	33.24	1
	Skin	0.831	23.83	1
	Fat1	0.005	1.104	1
	Fat2	0.050	1.592	1
	Fat3	0.080	3.545	1
	Fibro-glandular1	0.397	24.40	1
	Fibro-glandular2	0.738	35.55	1
	Fibro-glandular3	0.824	40.49	1
	Tumor	60	0.08	-0.005-0.008i

model II, respectively. The 2D views of the reconstructed images are represented in Figure 4(g) and Figure 4(h). It can be seen that the MNP target tumor can be identified in the reconstrued images with correct information on its shape, size, and position.

Breast models III and IV were developed using the MRI images from human subjects [33]. The breast model III consisted of a layer of muscle, skin, three types of fat tissue,

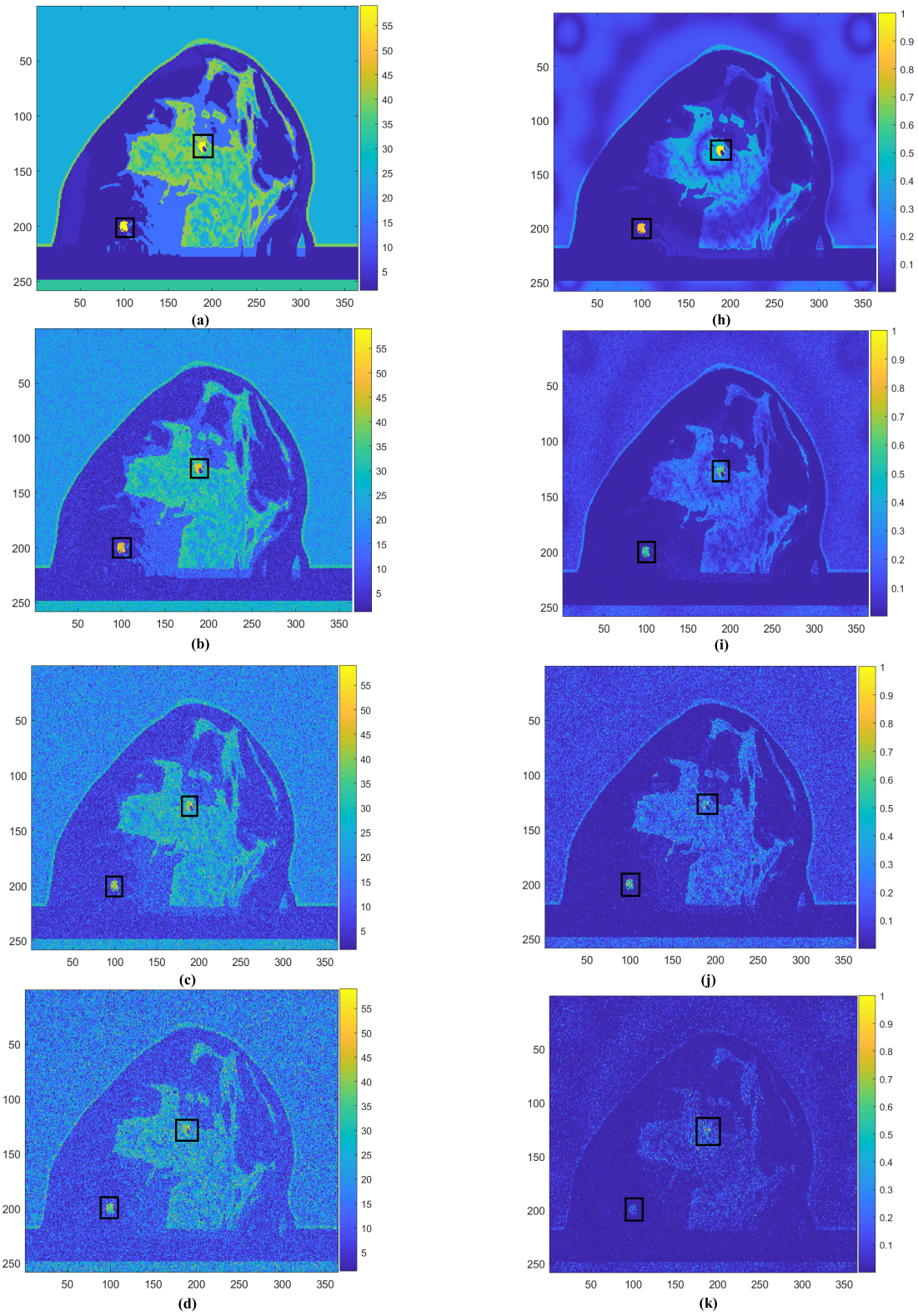

FIGURE 7. (a) 2D view of breast model IV (complex part); breast model IV with noises: (b) 5%; (c) 10%; (d) 15%; (e) 20%; (f) 30%; (g) 40%; reconstructed 2D images of breast model IV with noises: (h) 0%; (i) 5%; (j) 10%; (k) 15%; (l) 20%; (m) 30%; (n) 40%.

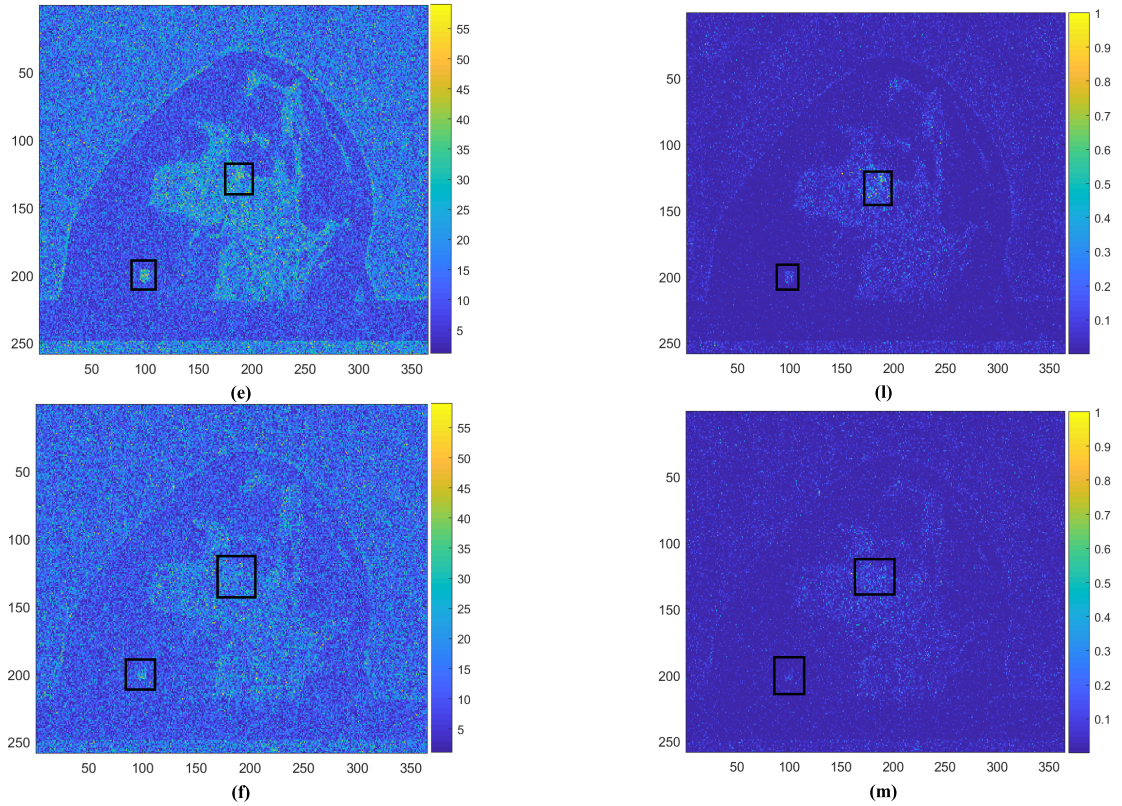

FIGURE 7. (a) 2D view of breast model IV (complex part); breast model IV with noises: (b) 5%; (c) 10%; (d) 15%; (e) 20%; (f) 30%; (g) 40%; reconstructed 2D images of breast model IV with noises: (h) 0%; (i) 5%; (j) 10%; (k) 15%; (l) 20%; (m) 30%; (n) 40%.

three types of fibro-glandular tissue, and one MNP target tumor ($\varepsilon_r = 60$, $\sigma_r = 0.8$ S/m, $\mu_r = -0.005 - 0.008i$). The tumor (189 mm, 128 mm, 124 mm) embedded in the fibro-glandular tissue. Figure 5(a) and Figure 5(d) shows the 3D and 2D views of the relatively permittivity and conductivity distributions of the breast model III, respectively. The 2D views of the real-part and imaginary-part of the permeability distributions of the breast model III are demonstrated in Figure 5(e) and Figure 5(f), respectively. Figure 5(g) and Figure 5(h) show the 2D views of the reconstructed images of the breast model III. The MNP target tumor could be observed in the reconstrued images with correct information on its shape, size, and position.

Breast IV was developed based on breast III but consisted of two MNP target tumors ($\varepsilon_r = 60$, $\sigma_r = 0.8$ S/m, $\mu_r = -0.005 - 0.008$i) with locations in (189 mm, 128 mm, 124 mm) and (100 mm, 200 mm, 124 mm) inside fibro-glandular tissue and fat tissue. Figures 6(a)-6(d) illustrates the 3D and 2D views of the real-part (relatively permittivity) and imaginary-part (conductivity) of breast model IV, respectively. The 2D views of the permeability distributions of the breast model IV are presented in Figures 6(e)-6(f). Figure 6(g) and Figure 6(h) shows the 2D views of the real-part and imaginary-part of the reconstructed images of the breast model IV. Two MNP target tumors could be detected in the real-part of the reconstructed images, but only one MNP target tumor could be observed in the imagery-part of the reconstructed images.

TABLE 2. PSNR of breast model IV with different percentages of noise.

Noise	0%	5%	10%	15%	20%	30%	40%
PSNR (dB)	21.09	20.87	20.29	19.46	18.53	16.67	14.87

Gaussian noises were added into the breast model to test the proposed method in a more realistic scenario. Figures 7(a)-(g) display the 2D views (complex-part) of the breast model IV with different percentages of noise, and Figures 7(h)-(n) present the reconstructed images breast model IV with different percentages of noise. It can be seen that the two MNP target tumors could be displayed in the reconstructed images when the breast model contains less than 30% noises, it is much easier to detect a tumor when it located inside fat tissue compared to fibro-glandular tissue and dense tissue. Table 2 demonstrates the PSNR values of the breast model IV with different percentages of noise.

In Figures 3-7, color bars in the real-part and imaginary-part of the breast models demonstrate the relative permittivity and conductivity distributions, respectively; color bars in the permeability distributions of the breast models demonstrate

the real-part and imaginary-part of the permeability distributions, respectively; while color bars in the reconstructed images describe the scalar values of the energy distributions, respectively.

VI. CONCLUSION

This paper reported the modeling of enhanced HMI for MNP target breast tumor detection. A numerical system, including a realistic breast model and image processing model, was developed to demonstrate the concept of the proposed framework. Wave propagation was included in the numerical system to model the dense breast. Equation (16) could be used to model the scattered electric field from the breast. Various numerical experiments were carried out to evaluate the accuracy, effectiveness, and sensitivity of the proposed method for detecting MNP target tumor in a dense breast under practical consideration. Both noise free and noise breast models were involved in this premilitary study.

Both noise free and noise models were involved in this study, and the breast image quality was degraded in the noise model. The breast image quality highly depends on the visibility data that compares the scattering signals measured by any pair of receivers. For 16-element transducer array with a fixed vertical location, a total number of 256 (16×16) scattered signals were measured to produce a 2D image.

The simulation results demonstrated that the MNP target tumors could be presented in the reconstructed breast image with correct information on its shape, size, and position. The tumors could be successfully observed in the breast images even when they located inside the dense tissue, such as the fibro-glandular tissue having the same DPs as a breast tumor. The proposed framework has the potential to become a helpful or alternative imaging tool for breast tumor detection in the future. However, the presented work leaks of experimental validations on more realistic scenarios. Future work includes the development of a prototype and tests the proposed framework on more realistic scenarios.

REFERENCES

[1] C. G. Yedjou *et al.*, "Assessing the racial and ethnic disparities in breast cancer mortality in the United States," *Int. J. Environ. Res. Public Health*, vol. 14, no. 5, p. 486, 2017.

[2] K.-J. Joo, J.-W. Shin, K.-R. Dong, C.-S. Lim, W.-K. Chung, and Y.-J. Kim, "A study on the dependence of exposure dose reduction and image evaluation on the distance from the dental periapical X-ray machine," *J. Korean Phys. Soc.*, vol. 63, no. 9, pp. 1824–1831, 2013.

[3] L. Wang, "Microwave sensors for breast cancer detection," *Sensors*, vol. 18, no. 2, p. 655, 2018.

[4] A. Zamani, S. A. Rezaeieh, and A. M. Abbosh, "Lung cancer detection using frequency-domain microwave imaging," *Electron. Lett.*, vol. 51, no. 10, pp. 740–741, 2015.

[5] F. Ye, Z. Ji, W. Ding, C. Lou, S. Yang, and D. Xing, "Ultrashort microwave-pumped real-time thermoacoustic breast tumor imaging system," *IEEE Trans. Med. Imag.*, vol. 35, no. 3, pp. 839–844, Mar. 2016.

[6] D. O'Loughlin, M. O'Halloran, B. M. Moloney, M. Glavin, E. Jones, and M. A. Elahi, "Microwave breast imaging: Clinical advances and remaining challenges," *IEEE Trans. Biomed. Eng.*, vol. 65, no. 11, pp. 2580–2590, Nov. 2018.

[7] A. Modiri, S. Goudreau, A. Rahimi, and K. Kiasaleh, "Review of breast screening: Toward clinical realization of microwave imaging," *Med. Phys.*, vol. 44, no. 12, pp. e446–e458, 2017.

[8] D. Ireland, K. Bialkowski, and A. Abbosh, "Microwave imaging for brain stroke detection using Born iterative method," *IET Microw. Antennas Propag.*, vol. 7, no. 11, pp. 909–915, Aug. 2013.

[9] L. Wang, "Electromagnetic induction holography imaging for stroke detection," *J. Opt. Soc. Amer. A, Opt. Image Sci.*, vol. 34, no. 2, pp. 294–298, 2017.

[10] S. Y. Semenov, A. E. Bulyshev, V. G. Posukh, Y. E. Sizov, T. C. Williams, and A. E. Souvorov, "Microwave tomography for detection/imaging of myocardial infarction. I. Excised canine hearts," *Ann. Biomed. Eng.*, vol. 31, no. 3, pp. 262–270, 2003.

[11] R. M. Irastorza, C. M. Carlevaro, and F. Vericat, "Is there any information on micro-structure in microwave tomography of bone tissue?" *Med. Eng Phys.*, vol. 35, no. 8, pp. 1173–1180, 2013.

[12] A. M. Hassan and M. El-Shenawee, "Review of electromagnetic techniques for breast cancer detection," *IEEE Rev. Biomed. Eng.*, vol. 4, pp. 103–118, Sep. 2011.

[13] H. Jiang, C. Li, D. Pearlstone, and L. L. Fajardo, "Ultrasound-guided microwave imaging of breast cancer: Tissue phantom and pilot clinical experiments," *Med. Phys.*, vol. 32, no. 8, pp. 2528–2535, 2005.

[14] R. Scapaticci, G. Bellizzi, I. Catapano, L. Crocco, and O. M. Bucci, "An effective procedure for MNP-enhanced breast cancer microwave imaging," *IEEE Trans. Biomed. Eng.*, vol. 61, no. 4, pp. 1071–1079, Apr. 2014.

[15] L. Wang, A. M. Al-Jumaily, and R. Simpkin, "Imaging of 3-D dielectric objects using far-field holographic microwave imaging technique," *Prog. Electromagn. Res. B*, vol. 61, pp. 135–147, Oct. 2014.

[16] L. Wang, A. M. Al-Jumaily, and R. Simpkin, "Investigation of antenna array configurations using far-field holographic microwave imaging technique," *Progr. Electromagn. Res. M*, vol. 42, pp. 1–11, Jun. 2015.

[17] R. Bardhan *et al.*, "Nanoshells with targeted simultaneous enhancement of magnetic and optical imaging and photothermal therapeutic response," *Adv. Funct. Mater.*, vol. 19, no. 24, pp. 3901–3909, 2009.

[18] Y. Liu *et al.*, "Magnetic nanoliposomes as *in situ* microbubble bombers for multimodality image-guided cancer theranostics," *ACS Nano*, vol. 11, no. 2, pp. 1509–1519, 2017.

[19] K. M. Krishnan, "Biomedical nanomagnetics: A spin through possibilities in imaging, diagnostics, and therapy," *IEEE Trans. Magn.*, vol. 46, no. 7, pp. 2523–2558, Jul. 2010.

[20] K. M. Krishnan, "Nanomagnetic materials in medicine: Recent developments in imaging, diagnostics and therapy," *Microscopy Microanal.*, vol. 22, no. S3, pp. 1228–1229, 2016.

[21] E. Pollert, P. Kaspar, K. Zaveta, V. Herynek, M. Burian, and P. Jendelova, "Magnetic nanoparticles for therapy and diagnostics," *IEEE Trans. Magn.*, vol. 49, no. 1, pp. 7–10, Jan. 2013.

[22] M. Stéphane, V. Sébastien, F. Grasset, and E. Duguet, "Magnetic nanoparticle design for medical diagnosis and therapy," *J. Mater. Chem.*, vol. 14, pp. 2161–2175, Jun. 2004.

[23] C. Felton, A. Karmakar, Y. Gartia, P. Ramidi, A. S. Biris, and A. Ghosh, "Magnetic nanoparticles as contrast agents in biomedical imaging: Recent advances in iron- and manganese-based magnetic nanoparticles," *Drug Metabolism Rev.*, vol. 46, no. 2, pp. 142–154, 2014.

[24] S. J. Norton and T. Vo-Dinh, "Imaging the distribution of magnetic nanoparticles with ultrasound," *IEEE Trans. Med. Imag.*, vol. 26, no. 5, pp. 660–665, May 2007.

[25] L. Zhang *et al.*, "High MRI performance fluorescent mesoporous silica-coated magnetic nanoparticles for tracking neural progenitor cells in an ischemic mouse model," *Nanoscale*, vol. 5, no. 10, pp. 4506–4516, 2013.

[26] G. Bellizzi, O. M. Bucci, and I. Catapano, "Microwave cancer imaging exploiting magnetic nanoparticles as contrast agent," *IEEE Trans. Bio-Med. Eng.*, vol. 58, no. 9, pp. 2528–2536, Sep. 2011.

[27] C. Leuschner, C. S. Kumar, W. Hansel, W. Soboyejo, J. Zhou, and J. Hormes, "LHRH-conjugated magnetic iron oxide nanoparticles for detection of breast cancer metastases," *Breast Cancer Res. Treatment*, vol. 99, no. 2, pp. 163–176, 2006.

[28] H. Amiri, K. Saeidi, P. Borhani, A. Manafirad, M. Ghavami, and V. Zerbi, "Alzheimer's disease: Pathophysiology and applications of magnetic nanoparticles as MRI theranostic agents," *ACS Chem. Neurosci.*, vol. 4, no. 11, pp. 1417–1429, 2013.

[29] F. Ul Amin *et al.*, "Osmotin-loaded magnetic nanoparticles with electromagnetic guidance for the treatment of Alzheimer's disease," *Nanoscale*, vol. 9, no. 30, pp. 10619–10632, 2017.

[30] G. Bellizzi, O. M. Bucci, and A. Capozzoli, "Broadband spectroscopy of the electromagnetic properties of aqueous ferrofluids for biomedical applications," *J. Magn. Magn. Mater.*, vol. 322, no. 20, pp. 3004–3013, 2010.
[31] P. C. Fannin, "Use of ferromagnetic resonance measurements in magnetic fluids," *J. Mol. Liquids*, vol. 114, pp. 79–87, Sep. 2004.
[32] P. C. Fannin, B. K. P. Scaife, A. T. Giannitsis, and C. M. Oireachtaigh, "High frequency ferromagnetic resonance measurements in magnetic fluids," *J. Magn. Magn. Mater.*, vol. 289, pp. 159–161, Mar. 2005.
[33] W. Zhang and Q. H. Liu, "Three-dimensional scattering and inverse scattering from objects with simultaneous permittivity and permeability contrasts," *IEEE Trans. Geosci. Remote Sens.*, vol. 53, no. 1, pp. 429–439, Jan. 2015.
[34] R. Levanda and A. Leshem, "Synthetic aperture radio telescopes," *IEEE Signal Process. Mag.*, vol. 27, no. 1, pp. 14–29, Jan. 2010.
[35] L. Wang and A. M. Al-Jumaily, "Imaging of lung structure using holographic electromagnetic induction," *IEEE Access*, vol. 5, pp. 20313–20318, 2017.
[36] E. Zastrow, S. K. Davis, M. Lazebnik, F. Kelcz, B. D. Van Veem, and S. C. Hagness. *Database of 3D Grid-Based Numerical Breast Phantoms for Use in Computational Electromagnetics Simulations*. Accessed: Feb. 6, 2019. [Online]. Available: http://uwcem.ece.wisc.edu/MRIdatabase/
[37] L. Josephson, C.-H. Tung, A. Moore, and R. Weissleder, "High-efficiency intracellular magnetic labeling with novel superparamagnetic-tat peptide conjugates," *Bioconjugate Chem.*, vol. 10, no. 2, pp. 186–191, 1999.
[38] Italian National Research Council. *An Internet Resource for the Calculation of the Dielectric Properties of Body Tissues in the Frequency Range 10 Hz-100 GHz*. Accessed: Feb. 6, 2019. [Online]. Available: http://niremf.ifac.cnr.it/tissprop

Authors' photographs and biographies not available at the time of publication.